



# Thermodynamic structure of supercritical LOX–GH<sub>2</sub> diffusion flames

Daniel T. Banuti<sup>a,\*</sup>, Peter C. Ma<sup>b</sup>, Jean-Pierre Hickey<sup>c</sup>, Matthias Ihme<sup>a,b</sup>

<sup>a</sup> Center for Turbulence Research, Stanford University, Stanford, CA 94305, USA

<sup>b</sup> Department of Mechanical Engineering, Stanford University, Stanford, CA 94305, USA

<sup>c</sup> Department of Mechanical and Mechatronics Engineering, University of Waterloo, Waterloo, ON N2L 3G1, Canada

## ARTICLE INFO

### Article history:

Received 26 September 2017

Revised 12 November 2017

Accepted 11 June 2018

### Keywords:

Counterflow diffusion flame

Flamelet

Transcritical

Supercritical

Injection

Rocket

## ABSTRACT

In this study, we evaluate the thermodynamic structure of laminar hydrogen/oxygen flames at supercritical pressures using 1D flame calculations and large-eddy simulation (LES) results. We find that the real fluid mixing behavior differs between inert (cold flow) and reactive (hot flow) conditions. Specifically, we show that combustion under transcritical conditions is not dominated by large-scale homogeneous real-fluid mixing: similar to subcritical atomization, the supercritical pure oxygen stream undergoes a distinct transition from liquid-like to gas-like conditions; significant mixing and combustion occurs primarily after this transition under ideal gas conditions. The joint study of 1D flame computations and LES demonstrates that real-fluid behavior is chiefly confined to the bulk LOX stream; real fluid mixing occurs but in a thin layer surrounding the LOX core, characterized by water mass fractions limited to 3%. A parameter study of 1D flame solutions shows that this structure holds for a wide range of relevant injection temperatures and chamber pressures. To analyze the mixing-induced shift of the local fluid critical point, we introduce a state-space representation of the flame trajectories in the reduced temperature and reduced pressure plane which allows for a direct assessment of the local thermodynamic state. In the flame, water increases the local mixture critical pressures, so that subcritical conditions are reached. This view of limited mixing under supercritical conditions may yield more efficient models and an improved understanding of the disintegration modes of supercritical flows.

© 2018 The Combustion Institute. Published by Elsevier Inc. All rights reserved.

## 1. Introduction

Injection at supercritical pressures is a technology ubiquitous in transportation; it is used in Diesel engines, gas turbines, and rocket engines [1,2]. At these conditions, subcritical break-up into ligaments and droplets, Fig. 1a, is replaced by a turbulent mixing process, Fig. 1b, when the surface tension vanishes under supercritical conditions [2–5].

However, a categorization based on the pure propellant critical pressures has been shown to be too simplistic: the critical pressure of a mixture may significantly exceed the critical pressures of the components [6], thus an injection process that is supercritical with respect to the injected fluid and the background gas, henceforth referred to as ‘nominally supercritical’, may still exhibit subcritical break-up characteristics. This has been demonstrated experimentally [7,8] and numerically [9–11].

The view of Fig. 1 has also informed the development of the respective numerical models: the sharp interfaces in subcritical

injection typically lead to an approach in which interfaces are tracked, whereas the diffuse mixing in supercritical injection is treated as a problem of accurately modeling the thermodynamics of the real fluid-state behavior and mixing. A ‘real fluid’ in this context is characterized by significant intermolecular forces that render the ideal gas equation of state inapplicable, consistent with the view in physical chemistry [12]. The canonical model was introduced by Oefelein and Yang [13].

This approach has been used extensively to study nominally supercritical combustion of liquid oxygen (LOX) with gaseous hydrogen (GH<sub>2</sub>), representative of liquid rocket engines. In such engines, the flame is anchored in a recirculation zone behind the LOX post of a coaxial injector [3,4,13]. Juniper et al. [14] noted that the quenching strain rate of a GH<sub>2</sub>/LOX flame exceeds the maximum values found in rocket engines by an order of magnitude. Indeed, it can be assumed in numerical modeling of rocket engines that the reactions reach a chemical equilibrium [15,16]. Experiments [3,4] and simulations [13,17,18] show that the flame effectively separates oxygen from hydrogen; the flame encloses the oxygen stream due to hydrogen-rich operating conditions. For specific flow conditions, combustion and mixing may take place in the ideal gas limit [19,20]. Thus, liquid propellant rocket engines

\* Corresponding author.

E-mail addresses: [daniel@banuti.de](mailto:daniel@banuti.de) (D.T. Banuti), [mihme@stanford.edu](mailto:mihme@stanford.edu) (M. Ihme).

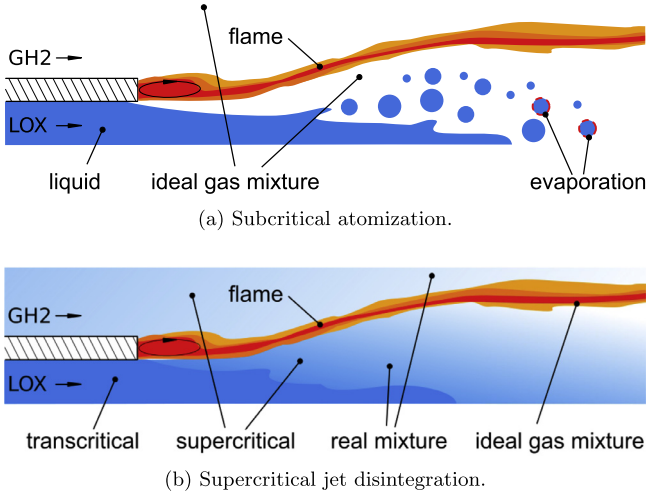


Fig. 1. Characterization of subcritical and supercritical injection.

exhibit combustion conditions that closely resemble idealized diffusion flames. Ribert et al. [21] and Pons et al. [22] used this insight to address counterflow diffusion flames under trans- and supercritical conditions, an approach that has since been adopted by other groups [23–25]. Since, large-eddy simulations (LES) of supercritical injection have become state-of-the-art [26,27], with fundamentals still being investigated [28,29].

Furthermore, ample evidence for a structure of the supercritical state space has been collected. Specifically, experimental [30,31] and theoretical [32,33] results indicate that distinct liquid-like and gas-like supercritical states can be distinguished. These states are separated by the Widom line, an extension to the coexistence line characterized by peaks in the isobaric specific heat capacity. The Widom line is a general fluid property [34] and can even be identified in mixtures [35]. The relevance of the Widom line for injection lies in pseudoboiling [2], the transition from liquid-like to gas-like supercritical states across the Widom line. Pseudoboiling resembles subcritical boiling, where a peak in the thermal expansivity causes a sudden drop in density, and a peak in isobaric specific heat capacity acts as an energy sink akin to the latent heat of vaporization [36]. Pseudoboiling has been identified as an important process in injection and combustion [23,37].

So far, a systematic investigation of the thermodynamic structure of supercritical non-premixed flames with respect to mixtures and transitions has not been carried out. Therefore, we address three questions in the present work: (1) In which part of the flame are real-fluid effects (pure fluid and mixing) relevant? (2) How does the local thermodynamic state and the critical point change throughout the flame? (3) How sensitive are these results with respect to changes in the injection conditions? To address these questions, we compute LES and 1D flame structures of the cryogenic LOX/GH<sub>2</sub> diffusion-flame at nominally supercritical pressure, covering inert and reactive cases. Variation of the 1D conditions over a range of strain rates from near-equilibrium to quenching conditions, pressures, injection temperatures, and dilution, are evaluated to assess the generality of the initial results. The spatial distribution of real fluid thermodynamics is demonstrated using LES results.

## 2. Numerical methods

This section discusses the numerical methods used for the present study. First, the thermodynamic model used for real fluid mixtures is introduced. The discussions of the 1D flame solver and

the LES solver, which use this thermodynamic model, follow. The section concludes with relations used in the analysis of the results.

### 2.1. Thermodynamic relations

The Peng–Robinson equation of state (PR EoS) [38] is used in this study for the evaluation of thermodynamic quantities. A cubic EoS has been chosen for its computational efficiency and readily available mixing rules; PR has been chosen for its accuracy especially for supercritical fluids [13]. Real-fluid effects are accounted for by departure functions that are derived from the state equation to ensure thermodynamic consistency of the governing equations. The PR state equation is expressed as

$$p = \frac{RT}{v-b} - \frac{a}{v^2 + 2bv - b^2}, \quad (1)$$

where  $R$  is the gas constant,  $v$  is the specific volume, and the coefficients  $a$  and  $b$  are functions of temperature and composition, accounting for effects of intermolecular attractive forces and volume displacement. For mixtures of  $N_s$  species, the coefficients  $a$  and  $b$  in Eq. (1) are evaluated as [6]

$$a = \sum_{\alpha=1}^{N_s} \sum_{\beta=1}^{N_s} X_{\alpha} X_{\beta} a_{\alpha\beta}, \quad (2a)$$

$$b = \sum_{\alpha=1}^{N_s} X_{\alpha} b_{\alpha}, \quad (2b)$$

where  $X_{\alpha}$  is the mole fraction of species  $\alpha$ . The coefficients  $a_{\alpha\beta}$  and  $b_{\alpha}$  are calculated using the mixing rules recommended by Harstad et al. [39], with

$$a_{\alpha\beta} = 0.457236 \frac{(RT_{cr,\alpha\beta})^2}{p_{cr,\alpha\beta}} \left[ 1 + c_{\alpha\beta} \left( 1 - \sqrt{T/T_{cr,\alpha\beta}} \right) \right]^2, \quad (3a)$$

$$b_{\alpha} = 0.077796 \frac{RT_{cr,\alpha}}{p_{cr,\alpha}}, \quad (3b)$$

$$c_{\alpha\beta} = 0.37464 + 1.54226\omega_{\alpha\beta} - 0.26992\omega_{\alpha\beta}^2. \quad (3c)$$

The critical properties of the major species are taken from the NIST database [40], the critical properties of the intermediate species are determined based on their Lennard–Jones potentials and their acentric factor is set to zero, following Giovangigli et al. [41]. The critical properties for all species considered in this study are compiled in Table 1.

In mixtures, the local critical pressure and temperature vary with composition. While the mixture critical temperature lies between the component pure fluid values, the mixture critical pressure may significantly exceed the pure fluid values. Both can be determined using the pseudocritical method described by Reid et al. [6], where

$$T_{cr,mix} = \sum_{\alpha=1}^{N_s} X_{\alpha} T_{cr,\alpha}, \quad (4a)$$

$$p_{cr,mix} = RT_{cr,mix} \frac{\sum_{\alpha=1}^{N_s} X_{\alpha} Z_{cr,\alpha}}{\sum_{\alpha=1}^{N_s} X_{\alpha} v_{cr,\alpha}}. \quad (4b)$$

The compressibility factor  $Z$  [6] is an important nondimensional parameter in real fluid thermodynamics, quantifying the deviation from ideal gas behavior. It is defined as

$$Z = \frac{pv}{RT}. \quad (5)$$

The critical compressibility factor  $Z_{cr}$  [6] corresponds to the compressibility factor evaluated for  $T_{cr}$ ,  $p_{cr}$ , and  $v_{cr}$ . Previous results

**Table 1**

Critical properties of species in H<sub>2</sub>/O<sub>2</sub> combustion, where  $T_{cr}$ ,  $p_{cr}$ ,  $v_{cr}$ , and  $\omega$  represent, respectively, the critical temperature, critical pressure, critical molar volume and acentric factor of the species.

Parameters	H <sub>2</sub>	O <sub>2</sub>	H <sub>2</sub> O	O	H	OH	H <sub>2</sub> O <sub>2</sub>	HO <sub>2</sub>	N <sub>2</sub>
$T_{cr}$ [K]	33.0	154.58	647.10	105.28	190.82	105.28	141.34	141.34	126.19
$p_{cr}$ [MPa]	1.284	5.043	22.064	7.088	31.013	7.088	4.786	4.786	3.395
$v_{cr}$ [cm <sup>3</sup> /mol]	64.28	73.37	55.95	41.21	17.07	41.21	81.93	81.93	89.41
$\omega$	-0.216	0.022	0.344	0.0	0.0	0.0	0.0	0.0	0.0372

[20] showed that the exact ideal gas condition  $\mathcal{Z} = 1$  is only met along a line in  $p_r - T_r$  space, implying that the ideal gas law is strictly not fulfilled for most practical CFD conditions. Allowing for a 5% deviation from ideal gas behavior, i.e.  $0.95 < \mathcal{Z} < 1.05$ , extends the quasi-ideal gas regime to practical values of  $p_r$  and  $T_r$ . Then, quasi-ideal behavior can be expected for  $T_r > 2$  and  $p_r < 3$ . For simplicity, we will refer to this as 'ideal' in the remainder of the paper.

## 2.2. CFD solver

The finite-volume solver CharLES<sup>x</sup> is used in this study. The numerical solver and the corresponding numerical methods are discussed in detail elsewhere [42–44], only a brief overview focusing on the models required for real fluids will be given here. The governing equations solved are the conservation of mass, momentum, energy, and species. The PR EoS, Eq. (1), is used to close the system. Details on how to evaluate thermodynamic quantities can be found in Ma et al. [43]. The dynamic viscosity and thermal conductivity are evaluated using Chung's method with high-pressure correction [45,46]. Takahashi's high-pressure correction [47] is used to evaluate binary diffusion coefficients. A diffuse interface method is used and no surface tension effects are considered.

The convective flux is discretized using a sensor-based hybrid scheme in which a high-order, non-dissipative scheme is combined with a low-order, dissipative scheme to minimize numerical dissipation [48]. A central scheme, which is fourth-order accurate on uniform meshes, is used along with a second-order ENO scheme for the hybrid scheme and a density sensor [42,43] is adopted in this study. An entropy-stable flux correction technique [43] ensures the physical realizability of the numerical solution including the positivity of scalars and the damping of non-linear instabilities in the numerical solution.

Transcritical flow is characterized by strong non-linearities inherent in the real-fluid EoS imposing severe numerical difficulties. To remedy spurious pressure oscillations generated by a fully conservative scheme [43,49], a double-flux method is extended to the transcritical regime [43]. A strong stability preserving 3rd-order Runge–Kutta (SSP-RK3) scheme [50] is used for time advancement, a Strang-splitting scheme [51] is applied in this study to separate the convection operator from the remaining operators of the system. For reacting cases, a transcritical extension of the flamelet/progress variable approach [52,53] is adopted [43,44].

## 2.3. Counterflow diffusion flame

The flamelet model [52,54] was found to be applicable to coaxial rocket injectors [23]. With this, a profile through a turbulent non-premixed flame can be represented by a 1D-counterflow diffusion flame. The axisymmetric, laminar counterflow diffusion flame admits a self-similar solution and can be simplified to a one-dimensional steady state problem [25,54]. The governing equations for continuity, radial momentum, species, and temperature can be written as

$$\frac{d}{dx}(\rho u) + 2\rho v = 0, \quad (6a)$$

$$\rho u \frac{dV}{dx} + \rho V^2 = \frac{d}{dx} \left( \mu \frac{dV}{dx} \right) - \Lambda, \quad (6b)$$

$$\rho u \frac{dY_\alpha}{dx} = -\frac{dJ_\alpha}{dx} + \dot{\omega}_\alpha, \quad (6c)$$

$$c_p \rho u \frac{dT}{dx} = \frac{d}{dx} \left( \lambda \frac{dT}{dx} \right) - \sum_{\alpha=1}^{N_s} J_\alpha \frac{dh_\alpha}{dx} - \sum_{\alpha=1}^{N_s} \dot{\omega}_\alpha h_\alpha, \quad (6d)$$

where conventional notation is used [25],  $V = w/r$ ,  $\Lambda = (\partial p/\partial r)/r$ ,  $h_\alpha$  is the sensible enthalpy of species  $\alpha$ , and  $J_\alpha = \rho Y_\alpha V_\alpha$  is the diffusion flux for species  $\alpha$ , accounting for multi-component diffusion [55]. The governing equations are closed with the PR EOS, discussed in Section 2.1. The mathematical boundary conditions are determined by the operating conditions of the engine, namely the propellant injection temperatures and the chamber pressure.

The governing equations and the equation of state are implemented in the CANTERA package [56]. Special care has been taken to fully resolve the thermodynamic nonlinearities of pseudoboiling near the Widom line [36] by modifying the grid adaptation strategy to account for the large variation in fluid properties.

A validation of the method with the detailed numerical simulation of a two-dimensional counterflow diffusion flame in the transcritical regime by Lacaze and Oefelein [23] was undertaken. The oxygen and hydrogen streams are injected at  $T_{LOX} = 120$  K and  $T_{GH2} = 295$  K, respectively, at a combustion pressure of 7.0 MPa. The strain rate, calculated as the velocity difference between the injectors divided by the separation distance [23], is  $10^5$  s<sup>-1</sup>.

We perform the comparison in composition space, using the definition of a mixture fraction based on atomic hydrogen mass fraction [23],

$$Z_H = W_H \left( 2 \frac{Y_{H_2}}{W_{H_2}} + \frac{Y_H}{W_H} + 2 \frac{Y_{H_2O}}{W_{H_2O}} + \frac{Y_{OH}}{W_{OH}} + \frac{Y_{HO_2}}{W_{HO_2}} + 2 \frac{Y_{H_2O_2}}{W_{H_2O_2}} \right), \quad (7)$$

where  $Y_\alpha$  and  $W_\alpha$  are mass fraction and molecular weight for species  $\alpha$ , respectively. In the pure LOX/GH2 case, the flame is situated at the stoichiometric mixture fraction  $Z_H = Z_{st} = 0.11$ .

Figure 2 shows temperature, composition, density, and specific heat capacity of the current simulation and the reference results. Mesh-convergence studies were performed to ensure that the solution is mesh independent. Results with and without Soret effect are presented. It can be seen that the Soret effect has a marginal but noticeable influence on all major flame properties, improving agreement with the reference solution, except for the lean temperature distribution. All 1D results presented in the following are simulated with the Soret effect taken into account. The real-fluid effects near the oxidizer injector are evidenced in Fig. 2c and d, showing profiles of density and heat capacity. The drop in density and the local peak in the specific heat capacity upon crossing the Widom line are well captured by the current model, as are the other flame properties.

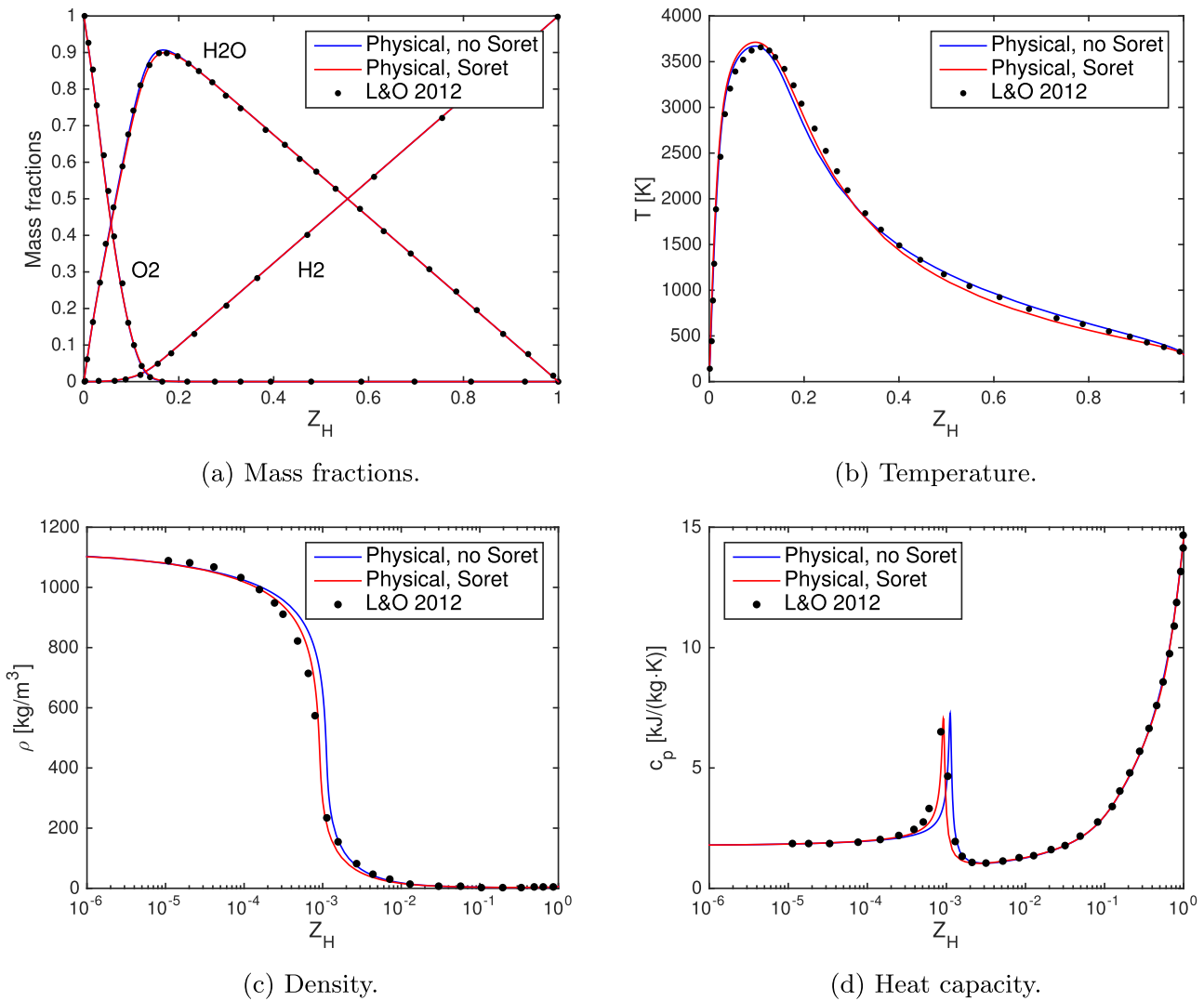


**Fig. 2.** Validation of the near-equilibrium flame (lines) with the detailed numerical simulation by Lacaze and Oefelein [23] (symbols). Baseline conditions are  $T_{LOX} = 120$  K,  $T_{GH2} = 295$  K,  $p = 7.0$  MPa.

### 3. Results

In this section, we discuss results of the 1D flame calculations with respect to the thermodynamic mixing behavior, and introduce a new diagram in terms of the local reduced pressure and reduced temperature, which allows an intuitive evaluation. To assess the generality, we then perform a parameter study in terms of strain rate, pressure, injection temperatures, and dilution of the fuel and the oxidizer stream. Finally, we analyze multidimensional CFD results and show that the conclusions from the 1D study are applicable to more complex approaches.

#### 3.1. Strain rate limits

We will first investigate how the limits of chemical equilibrium and quenching affect the overall flame structure for the baseline case introduced in Fig. 2 ( $T_{LOX} = 120$  K,  $T_{GH2} = 295$  K,  $p = 7.0$  MPa).

Figure 3 compares the structure of a near-equilibrium flame on the burning branch to the structure of a flame close to quenching, corresponding to the points on the top branch of the classical S-curve [54]. In the near-equilibrium case, hydrogen and oxygen mix only in a small region around  $Z_H = 0.11 = Z_{st}$ . The flame close to quenching conditions behaves very differently: oxygen and hydro-

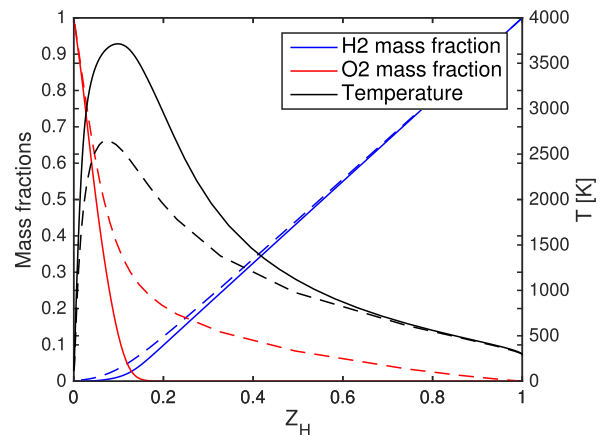


**Fig. 3.** Influence of strain rate on the 1D flame structure. Composition and temperature of near-equilibrium flame (solid line),  $\alpha = 1.0 \times 10^3$  1/s and of flame near quenching (dashed line),  $\alpha = 1.78 \times 10^7$  1/s.

gen are present throughout the composition space, the maximum temperature is reduced by more than 1000 K due to competition between heat release and diffusion.

### 3.2. Mixing and transition from a real to an ideal fluid

It is clear from Fig. 2c that the flame solution includes regions with liquid-like density in the oxidizer limit, and transitions to gaseous densities for higher mixture fractions. However, density at high pressures only indirectly yields information about the thermodynamic state. Furthermore, the actual composition at the transition is unclear. We will now investigate this in more detail.

Figure 4 shows profiles of the compressibility  $\mathcal{Z}$ , as well as mass fractions of hydrogen, oxygen, and water, for low strain rates and the near-quenching flame. At baseline conditions, real fluid behavior is observed only on the oxidizer side. For the condition near equilibrium, Fig. 4a shows how the compressibility factor reaches unity for  $Z_H > 2.0 \times 10^{-3}$ , while  $Y_{O_2}$  has only marginally reduced from unity. Near quenching, ideal gas conditions are reached at the slightly higher mixture fraction of  $Z_H > 3.0 \times 10^{-3}$ . Figure 4 shows the species mass fraction at which transition to an ideal gas occurs for  $H_2$ ,  $H_2O$ , and  $OH$ . In order to allow for a quantitative evaluation of the purity of oxygen at the transition,  $(1 - Y_{O_2})$  is shown instead of  $Y_{O_2}$ . The curves for  $Y_{H_2O}$  and  $(1 - Y_{O_2})$  are indistinguishable, indicating that  $Y_{H_2O} + Y_{O_2} \approx 1$  during conversion to ideal gas conditions; the radicals remain confined to the reaction zone. We obtain a water mass fraction of  $\approx 2\%$  at the transition to an ideal gas. Only traces of  $H_2$  and  $OH$  are present as real fluids, with mass fractions four orders of magnitude less than that of water. We can conclude that the transition from dense transcritical oxygen to an ideal gas occurs under almost pure conditions in equilibrium flames. This is consistent with earlier results [20].

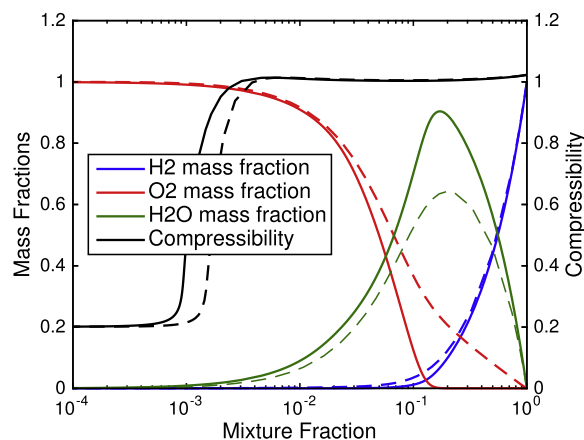
We will now evaluate the supercritical transition of liquid-like oxygen to gaseous supercritical oxygen in more detail. Figure 2c shows a very steep change in density at  $Z_H \approx 1.0 \times 10^{-3}$ , accompanied by a distinct maximum in isobaric specific heat capacity, as shown in Fig. 2d. This peak has been identified as a main effect hindering the heating of the LOX core by acting as a thermal barrier [23] and causing an increased thermal sensitivity in pure fluid injection [37]. It is thus important to identify the origin of the  $c_p$  peak in the context of diffusion flames. Earlier studies associated the peak in heat capacity to the mixture reaching the mixture critical temperature [18] or the transcritical nature of the fluid [23].

We have seen that the transition of dense oxygen to an ideal gas at baseline conditions occurs almost as a pure fluid, specifically, in a binary mixture of oxygen and water with a water mass fraction of  $\approx 2\%$ . Significant fractions of both components have to be present at the mixture critical temperature for high pressure phase separation to occur (in the  $H_2/O_2$  system investigated by Yang [18], the critical mixture temperature at  $p = 8$  MPa is reached for an oxygen mole fraction of 0.8). These conditions are not met in the present case. Instead, we recognize the  $c_p$  peak as an instance of pseudoboiling [2,36], the transition from a supercritical liquid-like to a gas-like state involving a rapid expansion and reduced temperature increase when heat is added, albeit over a finite temperature interval.

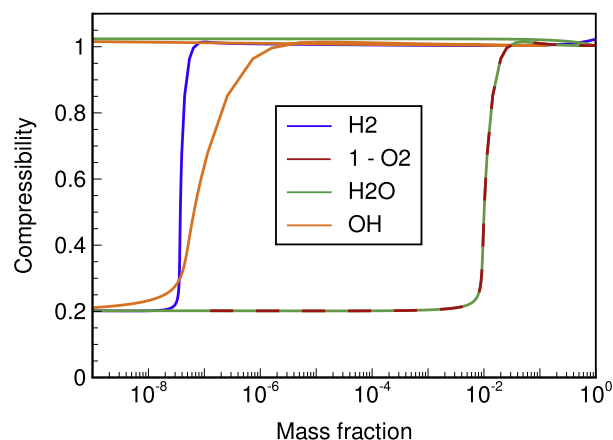
### 3.3. The reduced state plot as system representation

After studying the transition from a real to an ideal fluid in the cryogenic limit, we now proceed to examine the thermodynamic trajectory of the whole flame solution. The goal is to extend the approach of Lacaze and Oefelein [23] by introducing a more intuitive representation, and then to evaluate the generality of the results via a parametric study.

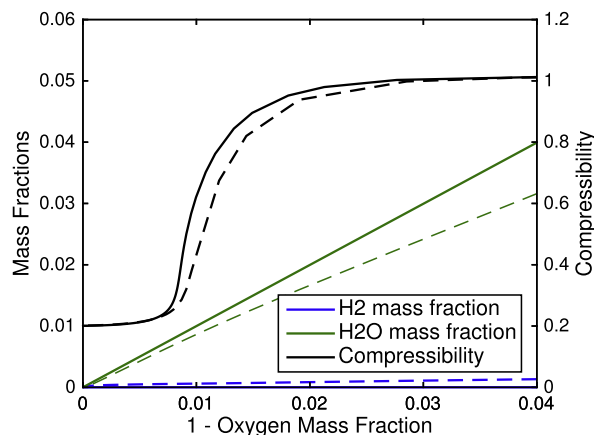
The critical point of a mixture may deviate substantially from the critical point of its constituents and can be calculated using the mixing rules of Eqs. (4a) and (4b). In order to evaluate the profile of the thermodynamic state, Dahms et al. [57] introduced plots of reduced temperature  $T_r = T/T_{Cr}$  and reduced pres-



(a) Mass fraction and compressibility plotted against mixture fraction.



(b) Congruency of  $\mathcal{Z}(Y_{H_2O})$  and  $\mathcal{Z}(1 - Y_{O_2})$  in near-equilibrium flame shows that the real-fluid transitions into an ideal gas as a binary mixture. Only traces of the other species are present at the transition, e.g. hydrogen and hydroxyl.



(c) Linear scale shows that the transition to an ideal gas occurs as a binary water/oxygen mixture.

**Fig. 4.** Species mass fractions and compressibility factor for equilibrium (solid) and near-quenching (dashed) flame. In the equilibrium case,  $\mathcal{Z} \approx 1$  for  $Z_H > 2.0 \times 10^{-3}$ , for near quenching at  $Z_H > 3.0 \times 10^{-3}$ . Evaluation in terms of deviation from oxygen mass fraction reveals that only water mixes with oxygen under real-fluid conditions in the equilibrium case.

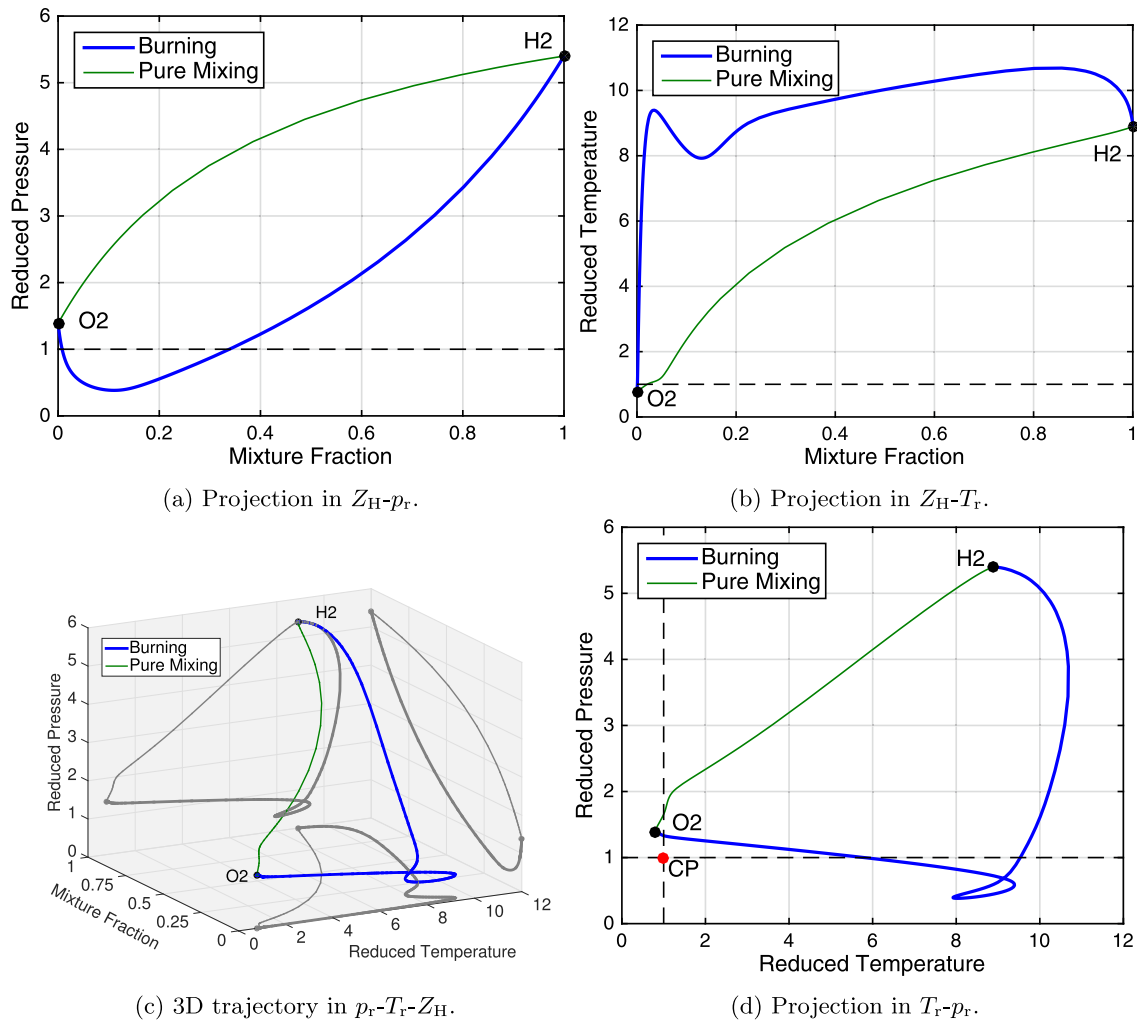


Fig. 5. Projections of the flamelet trajectories in  $Z_H - p_r - T_r$  - space, evaluated for baseline conditions (Fig. 2).

sure  $p_r = p/p_{cr}$  versus mixture fraction to analyze mixture profiles. Only when reduced pressure and reduced temperature are simultaneously smaller than unity, subcritical phase separation is possible. Lacaze and Oefelein [23] applied this approach to reactive mixtures. Figure 5a and b shows results for the investigated conditions near equilibrium and for inert mixing, neither of which indicates phase separation.

Interpretation of Fig. 5a and b is not straightforward, even though each graph represents but a single operating condition in terms of injection temperature and chamber pressure. Furthermore, it is not obvious how changes in operating conditions will affect the thermodynamic structure. There is a more intuitive way of representing the data by collapsing the mixture fraction in both plots and combining them in a reduced pressure/reduced temperature diagram, as shown in Fig. 5d. In this graph, every flamelet corresponds to a trajectory in the  $T_r - p_r$  state space obtained from Eqs. (4a) and (4b), connecting the oxidizer and fuel injection states 'O2' and 'H2' for a specific set of boundary conditions. Then, the criterion for identifying a phase change is straightforward: it will occur when the thermodynamic trajectory intersects the coexistence line. Consequently, when a trajectory passes the critical point at supercritical pressure, the mixing rules predict that no phase separation occurs, as the trajectory does not intersect the coexistence line.

Any variation of the reduced pressure is a function of only the local composition when the combustion pressure is kept constant.

Variations of the reduced temperature are caused by both changes in temperature and in composition. Thus, horizontal parts of the trajectory would mark regions where the fluids heat without a change in composition.

Figure 5d combines a trajectory near chemical equilibrium (blue), and an inert mixing line (green), for the baseline operating condition ( $T_{LOX} = 120$  K,  $T_{GH2} = 295$  K,  $p = 7.0$  MPa). No phase separation is predicted in either case. For the flame solution, oxygen is seen to heat with limited mixing, until a loop is formed at subcritical pressures. This loop is caused by the presence of water in the reaction zone, which significantly changes the local critical parameters due to its comparatively high critical pressure and temperature, see Table 1. Towards the pure hydrogen limit, the reduced temperature reaches a maximum. The inert mixing case constitutes a monotonic trajectory, with an inflexion point close to the critical temperature. It is interesting to note that the inert cryogenic mixing case passes the critical temperature at a higher reduced pressure than the reactive flamelet and thus appears less susceptible to phase separation.

Figure 5d is useful for a number of reasons. First, it allows for the direct assessment as to whether the coexistence line is crossed or not instead of inferring this from two graphs as in Fig. 5a and b. Second, it can combine several flamelet trajectories, without affecting readability. This means that it not only highlights a singular condition, but instead may be used to assess the physical envelope of an engine in the  $p_r - T_r$  phase space, as determined

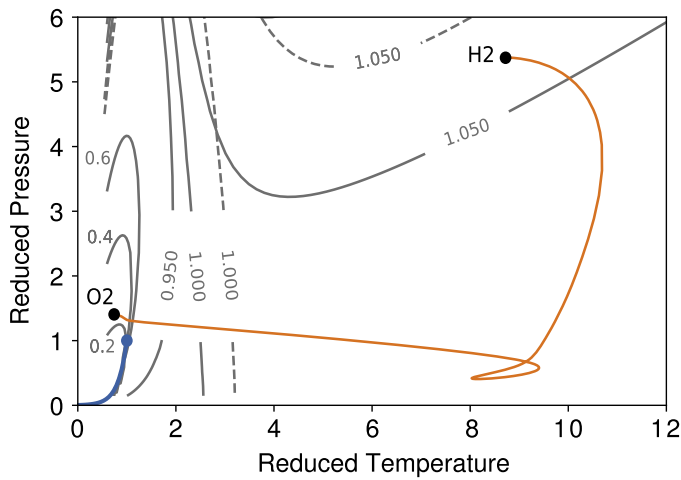


**Fig. 6.** Flame structure trajectory between pure oxygen and pure hydrogen in terms of the local reduced pressure and temperature. Gray contours mark the compressibility  $z$  for oxygen (solid) and hydrogen (dashed). The blue line is the coexistence line. Data are evaluated from NIST [40].

by the chamber pressure and the injection conditions for LOX and GH<sub>2</sub>. Third, the plot allows to develop intuition as to what effect a change in operating conditions has on the trajectories.

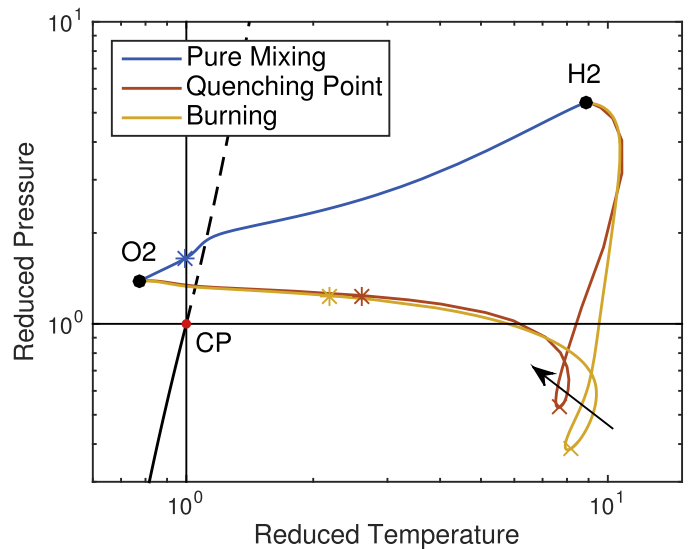
### 3.3.1. Analysis of the thermodynamic structure

The previous section introduced the  $T_r - p_r$  reduced state plot as a way to assess local flame conditions, but left a number of details unclear, such as the nature of the nonlinearity of the inert mixing line upon crossing  $T_{cr}$ , or the actual position of the flame in the plot. We will proceed by performing a more detailed analysis to examine these aspects further.

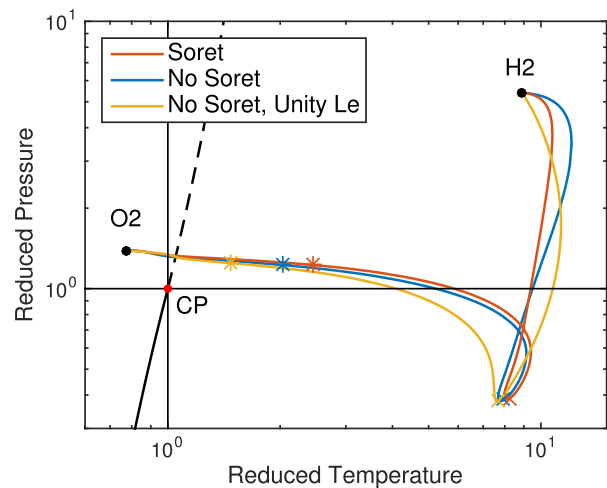
Figure 6 shows the trajectory of a flame at baseline conditions with the fluid compressibility superimposed. Oxygen is injected in a liquid-like state with  $z \approx 0.2$ . When the temperature of the flame increases by heat diffusion from the flame, ideal gas behavior is reached for  $T_r > 2$ , consistent with earlier results [20]. The dashed contours show that hydrogen reaches ideal gas conditions at higher temperatures and sustains ideal gas behavior for higher pressures. We can see that the reduced conditions of the hydrogen injection correspond to ideal gas behavior for hydrogen, but would show emerging real fluid behavior for oxygen.

Figure 7 is an extension of Fig. 5d, adding the point of maximum temperature ( $\times$ ), the point where the oxygen mass fraction drops to 0.98 ( $*$ ), the coexistence line (solid line), and the Widom line (dashed line). Different fluids may exhibit different Widom lines [34], however, due to the predominant presence of oxygen when the Widom line is crossed by the state trajectory, we show the Widom line of oxygen. The arrow points in the direction of an increasing value of the parameter. In Fig. 7, this parameter is the strain rate, we add the flamelet trajectory corresponding to the near-quenching point.

Counterintuitively, hot reacting cases are more prone to phase separation than cryogenic inert mixing, judged by the reduced pressure when passing the critical temperature. This can be attributed to the formation of water in the flame, which significantly influences the mixture critical properties due to its comparably high  $T_{cr}$  and  $p_{cr}$ , see Table 1. In turn, the resulting reduced pressures decrease, pushing the trajectories closer to the critical point. This effect of water is strongest where the highest temperatures are reached, pushing the associated loop in the trajectory to reach even subcritical pressures: the highest temperature is not found at the highest reduced temperature, but instead near the lowest reduced pressure. The highest reduced temperature is in-



**Fig. 7.** Flame structure trajectories between pure oxygen and pure hydrogen in terms of the local reduced pressure and temperature. The asterisk ( $*$ ) denotes an oxygen mass fraction of 0.98, the cross ( $\times$ ) marks the state of highest temperature; black solid and dashed lines are the coexistence line and pseudoboiling line, respectively, separated by the critical point (CP).



**Fig. 8.** Effect of transport model on flame trajectory.

stead found on the rich side of the flame, and caused by the very low critical temperature of hydrogen. For the reactive cases, oxygen is heated by thermal diffusion from the reaction zone to temperatures exceeding  $2T_{cr}$ , thus reaching ideal gas conditions before significant mixing occurs. In the cold mixing case, however, hydrogen is found to diffuse into the dense liquid oxygen in a non-ideal mixing process. Indeed, the horizontal part of the trajectory near pure oxygen conditions indicates an interesting physical phenomenon: for constant combustion pressures, the reduced pressure only changes with the composition according to Eq. (4b). Then, horizontal parts of the trajectory signify regions in which heat transfer occurs with very limited mixing. This corresponds to high Lewis numbers in near-critical fluids, consistent with results of Harstad & Bellan [58] and Lacaze & Oefelein [23].

Figure 8 demonstrates the influence of the transport model on the thermodynamic flame structure in more detail. In contrast to the noticeable effect of including the Soret term on the temperature and density distributions, shown in Fig. 2, the fuel-rich side of the flame trajectory in Fig. 8 is significantly modified. Assuming a

unity Lewis number is furthermore found to overestimate diffusive mixing towards the cryogenic oxygen stream.

### 3.3.2. Effect of parameter variations

We extend our analysis by considering effects of operating conditions and propellant dilution on the state-space representation. Figure 9a shows the impact of combustion pressure on the trajectories. Increasing the pressure mainly leads to a translation of the curves towards higher reduced pressures, as the fluid critical pressures and the composition remain approximately constant. While the maximum temperature increases with pressure, this effect is hardly discernible. A slight drop in reduced pressure moving away from the pure oxygen condition can be seen prior to reaching the Widom line; both move to higher temperatures as the pressure is increased. The dilution of the oxygen stream (\*) is not affected by a variation in pressure.

The impact of the oxidizer temperature on the trajectories is shown in Fig. 9b. The fuel-rich side from pure hydrogen to the flame loop at the highest temperature remains essentially unchanged, the oxygen side of the flame is translated to higher reduced temperatures upon raising the oxygen temperature. The bottom of the flame loop is hardly affected: while a higher oxygen temperature provides a higher enthalpy which in turn raises the combustion temperature, this effect is practically negligible compared to the heat released in the flame.

Variation of the fuel temperature is shown in Fig. 9c. The oxidizer side of the flame remains unchanged, while the pure hydrogen boundary condition moves to lower reduced temperatures as the hydrogen temperature is decreased. The lower the hydrogen temperature, the longer is the horizontal initial part of the flamelet trajectory emanating from the hydrogen injection condition, signifying heating without mixing. The impact of the hydrogen temperature on the flame position is visible, and can be attributed to the higher heat capacity of hydrogen and the larger temperature interval compared to the oxidizer variation shown in Fig. 9b.

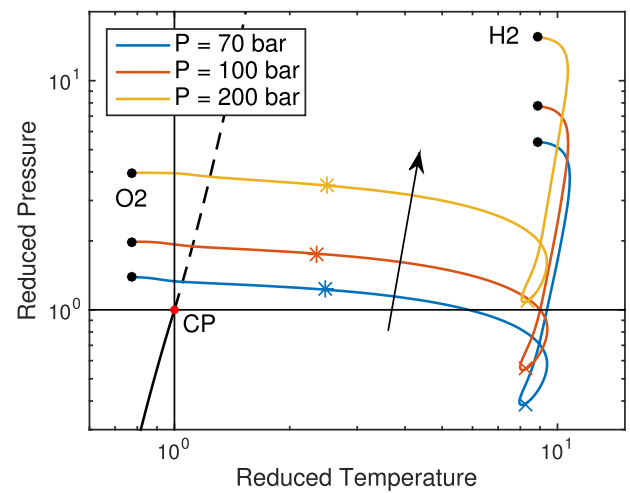
Finally, we study the effect of diluting the propellant streams, using nitrogen in the oxidizer flow (representative for air-breathing combustion), and water in the fuel stream (representative for pre-burner combustion). Figure 10 shows how an increasing nitrogen fraction in the oxidizer stream affects the thermodynamic structure of the flame. Due to the lower critical temperature and pressure of nitrogen compared to oxygen, we see in Fig. 10a how the oxidizer injection condition moves towards higher reduced pressures and temperatures as the mass fraction is increased. The flame loop narrows and shifts to higher reduced pressures, before vanishing altogether as the composition of air is approached. The maximum flame temperature is reduced, the temperature peak moves to lower mixture fractions as the stoichiometric mixture ratio shifts, see Fig. 10b.

Addition of water to the hydrogen stream can be evaluated from Fig. 11. Figure 11a shows that the reduced state of the injection condition shifts with diluent mass fraction. Due to the large critical properties of water, the effect is more pronounced than for the oxygen dilution case – the fuel injection point eventually reaches subcritical pressures. The flame loop opens and moves to lower reduced temperatures. The maximum temperature of the flame reduces with diluent mass fraction, and shifts to higher mixture fractions, see Fig. 11b.

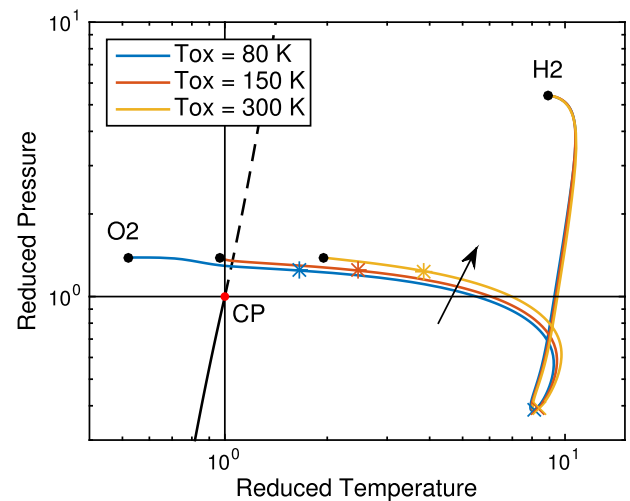
We can conclude that changes in the boundary conditions do indeed lead to well behaved variations in the flame trajectories that allow to develop intuition.

### 3.4. Application to multidimensional simulation results

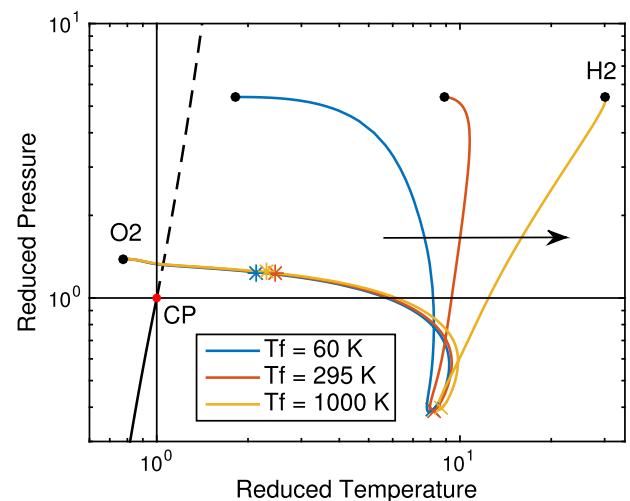
In order to allow for an assessment of the spatial thermodynamic structure, we analyze the LOX/GH<sub>2</sub> shear layer configura-



(a) Variation of pressure.



(b) Variation of oxygen temperature.



(c) Variation of hydrogen temperature.

**Fig. 9.** Flame structure trajectories between pure oxygen and pure hydrogen in terms of the local reduced pressure and temperature. Shown are variations of pressure, and the impact of varying oxidizer and fuel temperature. The asterisk (\*) denotes an oxygen mass fraction of 0.98, the cross (x) marks the state of highest temperature; black solid and dashed lines are the coexistence line and the oxygen Widom line, respectively.

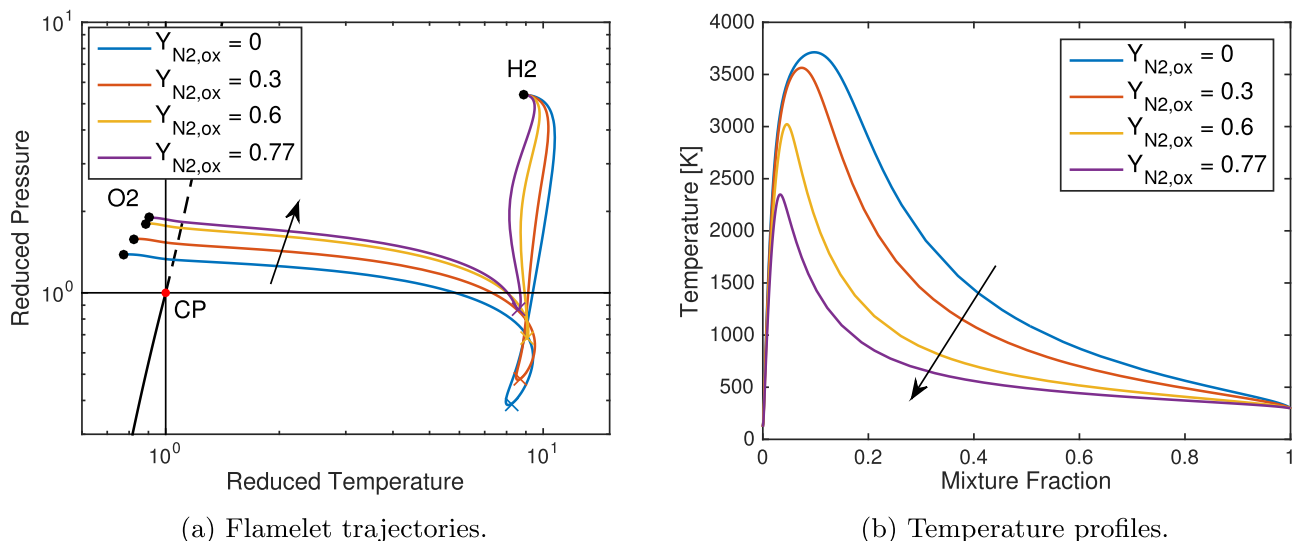


**Fig. 10.** Flame trajectories between oxidizer and pure hydrogen in terms of the local reduced pressure and temperature. Shown is the effect of added nitrogen in the oxidizer stream. The (x) marks the state of highest temperature; black solid and dashed lines are the coexistence line and oxygen Widom line, respectively. Pressure and inflow temperatures are identical to the baseline case.

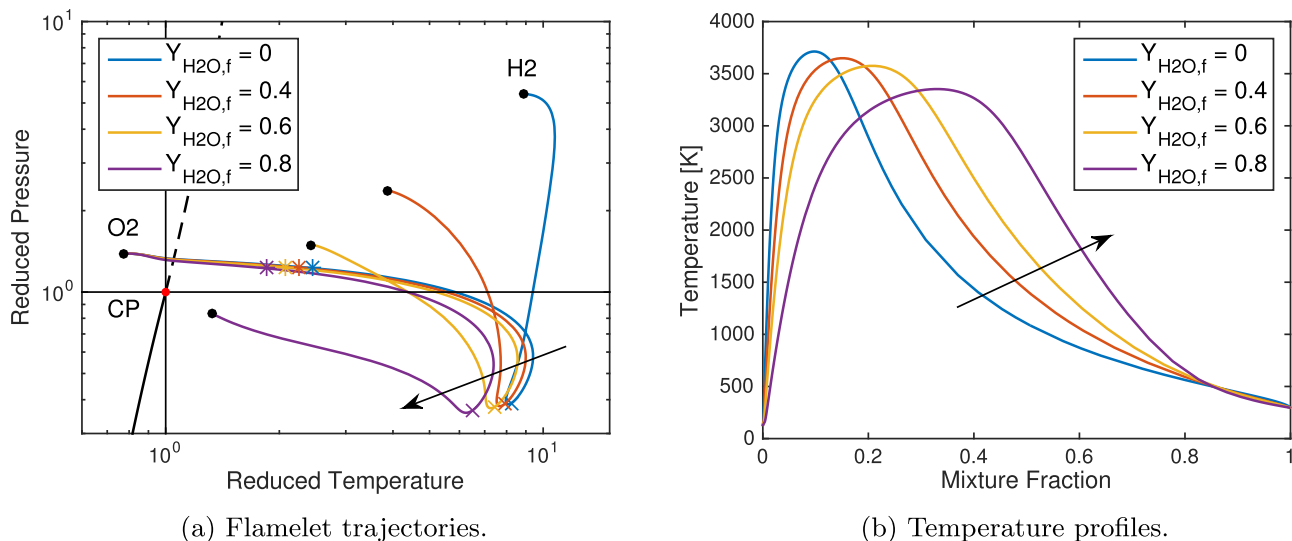


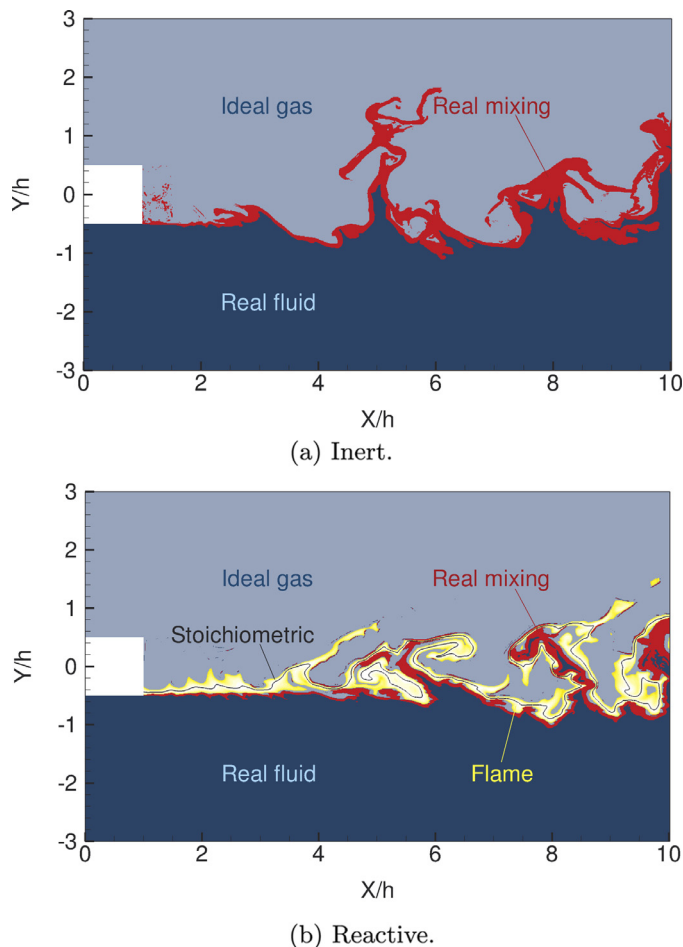
**Fig. 11.** Flame structure trajectories between pure oxygen and fuel in terms of the local reduced pressure and temperature. Shown is the effect of added water in the fuel stream. The (x) marks the state of highest temperature; black solid and dashed lines are the coexistence line and oxygen Widom line, respectively.

tion that has been proposed as a benchmark case by Ruiz et al. [59]. The computational domain is 2D, thus a realistic structure of turbulent flow features cannot be expected, however, we are interested here in the local mixing behavior, which we expect to not be affected by the 2D domain. The case is set up as follows: The LOX stream is injected at a temperature of 100 K, and GH2 is injected at a temperature of 150 K, at a chamber pressure of 10 MPa. The operating conditions are purely supercritical for the hydrogen stream and transcritical for oxygen. The GH2 and LOX jets have velocities of 125 m/s, and 30 m/s, respectively. Simulations are performed using the method described in Section 2.2. The two streams are separated by an injector lip of height  $h = 0.5$  mm, which is also included in the computational domain. The region of interest extends from 0 to  $10h$  in the axial direction with the origin set at the center of the lip face. A sponge layer of length  $5h$  at the end of the domain is included to absorb acoustic waves. The computational mesh has 100 grid points across the injector lip. A uniform mesh is used in both directions for the region from 0 to  $10h$  in axial direction and from  $-1.5h$  to  $1.5h$  in transverse direction; stretching

is applied with a ratio of 1.02 only in the transverse direction outside this region. Adiabatic no-slip wall conditions are applied at the injector lip and adiabatic slip wall conditions are applied for the top and bottom boundaries of the domain. A 1/7th power law for the near-wall velocity profiles is used for both the LOX and GH2 streams. The CFL number is set to 0.8 and no sub-grid scale model is used.

### 3.4.1. Flow field

Oefelein [19] carried out a thorough analysis of spatial profiles of this case. In particular, profiles of the compressibility factor and the density demonstrate the thin region in which the transition from a liquid-like to a gas-like supercritical fluid occurs. We extend this work by analyzing the complete 2D region of interest with regard to its thermodynamic characteristics. Specifically, we identify regions of real fluid behavior under the criterion that the local compressibility factor, as introduced in Eq. (5), is unity  $\pm 5\%$ . We identify real fluid mixing when the local fluid behaves like a real fluid and more than one species is present in a significant fraction.



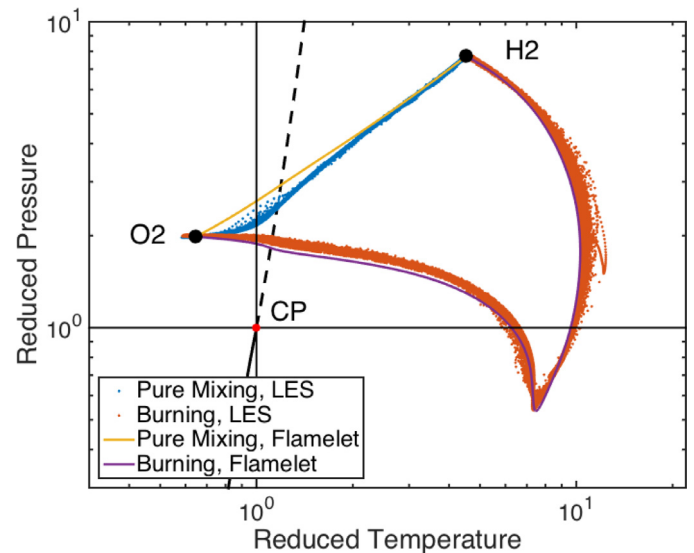
**Fig. 12.** Domains of inert and reactive LOX (bottom stream) GH2 (top stream) shear layers at nominally supercritical pressure. Light and dark blue denote ideal gas ( $0.95 < Z < 1.05$ ) and real fluid behavior ( $Z < 0.95 \vee Z > 1.05$ ), respectively. Real mixing ( $Z < 0.95 \wedge Y_{O_2} < 0.999$ ) is marked red, the flame ( $T > 2000$  K) is yellow. The black line corresponds to the stoichiometric mixture fraction  $Z_{H, st} = 0.11$ . (For interpretation of the references to color in this figure legend, the reader is referred to the web version of this article).

Figure 12 shows the flow fields of the inert and the reactive computation. In both cases, the GH2 stream (on top) can be considered an ideal gas, whereas LOX (on the bottom) behaves like a real fluid. In the inert case in Fig. 12a, real mixing occurs mainly in a layer between the streams, some cells with real mixing can be seen in the recirculation zone behind the injector lip. Figure 12b shows that the real mixing layer in the reacting case is thinner and clearly separated from the stoichiometric line. In some positions, localized regions of real mixing can be observed on the fuel-rich side of the flame.

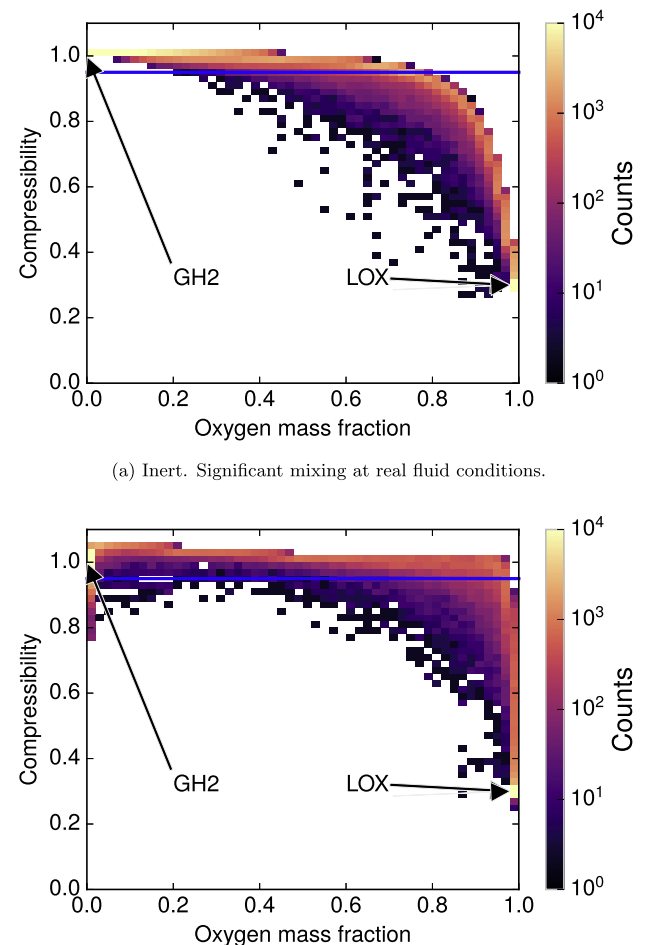
#### 3.4.2. Mixing analysis

Figure 13 is the reduced state plot for the CFD shear layer, capturing the characteristics of the 1D flame solutions. The result matches the unity Lewis number 1D flame solution shown in Fig. 8, most notably in the absence of the flame loop. More importantly, no significant reduction in the reduced pressure is observed during the bulk transition from real fluid to ideal gas conditions, consistent with the 1D results.

A more quantitative view of real fluid mixing is provided by Fig. 14. It shows the count of cells, representative of computational cost, for a given compressibility - oxygen mass fraction combination, for a given compressibility - oxygen mass fraction combination. Figure 14a indicates that in the inert case, more than 20% dilutant has to be mixed with oxygen before an ideal gas state is



**Fig. 13.** Flame structure trajectories between pure oxygen and pure hydrogen in terms of the local reduced pressure and temperature from LES results of a LOX/GH2 shear layer calculation.



**Fig. 14.** Scatter plots of ideal to real fluid transition in terms of oxygen mass fraction and compressibility factor. LOX and GH2 denote the respective inflow conditions, which exceed a count of 400,000 each and are capped here to improve readability. The trace of orange fields thus represents the main mixing trajectory. The horizontal line represents the  $Z > 0.95$  threshold to ideal gas conditions. The bin size is 0.02 in both dimensions.

reached, i.e. significant mixing under real conditions occurs. Under reactive conditions, Fig. 14b shows that oxygen heats up, reducing the compressibility factor, without significant mixing. In fact, the main mixing line reaches ideal gas conditions for an oxygen mass fraction of 0.96.

Figure 7 showed that substantial mixing among inert gases occurs under real fluid conditions, whereas in the reactive case, mixing is limited before the transition to ideal gases occurs, explaining the thicker inert real mixing layer. Furthermore, water diffusing into the hydrogen stream will tend to bring the fluid state closer to real fluid conditions, Fig. 11a, explaining the fuel-side real fluid region in the LES.

### 3.5. A proxy for real fluid behavior

Figure 14 provides a perspective of mixing, ideal-to-real transition, and the difference between the inert and the reactive case. The dependence on the oxygen mass fraction suggests the question as to whether we could use it as a proxy to identify real fluid behavior: the oxygen mass fraction is a known variable in a solver and could be used to predict on a cell-to-cell basis whether a real fluid model is required. We address two questions: Where do we need a model for real fluids? and Where do we need a model for real mixing? We seek to maximize the number of true positives, i.e. cells which we correctly predict as real fluids, and to minimize the number of false positives, i.e. cells which we treat as real fluids but do indeed obey ideal gas behavior. To this end, we label each computational cell with  $0.95 < Z < 1.05$  as ideal, and as real otherwise. We introduce the cut-off oxygen mass fraction  $Y_{O_2}^{\text{cutoff}}$  such that we only include the cells with  $Y_{O_2} > Y_{O_2}^{\text{cutoff}}$ . We furthermore introduce  $\phi_{\text{real}}^{\text{TP}}$  and  $\phi_{\text{real}}^{\text{FP}}$  as the predicted true positive and false positive real fluid fraction.

Consider the case in which the flow field consists exclusively of cells that either contain ideal pure hydrogen, or real pure oxygen. Then,  $\phi_{\text{real}}^{\text{TP}} = 1, \forall Y_{O_2}^{\text{cutoff}} \in \{0, 1\}$  and the accuracy of our prediction is 1.0. We would also capture all real fluid cells if some cells contained only ideal pure oxygen ( $\phi_{\text{real}}^{\text{TP}} = 1, \phi_{\text{real}}^{\text{FP}} > 0$ ). It is furthermore possible that (i) cells behave as real fluids that do not contain any oxygen ( $Y_{O_2}^{\text{cutoff}} \rightarrow 0: \phi_{\text{real}}^{\text{TP}} < 1$ ), (ii) cells behave as real fluids real that contain diluting species in addition to oxygen ( $Y_{O_2}^{\text{cutoff}} \rightarrow 1: \phi_{\text{real}}^{\text{TP}} < 1$ ). In the former case we make an error while evaluating the cell, in the latter case we need a real mixing model in addition to the real fluid property model.

Figure 15 shows the real fluid fractions  $\phi_{\text{real}}^{\text{TP}}$  and  $\phi_{\text{real}}^{\text{FP}}$  as a function of the cut-off oxygen mass fraction  $Y_{O_2}^{\text{cutoff}}$  for the inert and the reactive shear layer. In the inert case,  $Y_{O_2} > 0$  is a proxy that captures all real fluid cells ( $Y_{O_2}^{\text{cutoff}} \rightarrow 0: \phi_{\text{real}}^{\text{TP}} = 1$ ), while this is not the case for the reactive shear layer: cells containing water on the hydrogen side of the flame also behave real, as can be seen in Fig. 12b, amounting to a 1% error. However, for  $Y_{O_2}^{\text{cutoff}} \rightarrow 0$  more and more ideal cells are erroneously classified as real,  $\phi_{\text{real}}^{\text{FP}} > 0$ . As  $Y_{O_2}^{\text{cutoff}}$  increases,  $\phi_{\text{real}}^{\text{FP}}$  decreases and eventually drops to zero at  $Y_{O_2}^{\text{cutoff}} \approx 0.75$  for the inert case, and  $Y_{O_2}^{\text{cutoff}} \approx 0.97$  for the reactive case. Thus, as an answer to the first question, we can summarize that for the inert case,  $Y_{O_2} > 0.75$  proves to be an acceptable criterion that captures 99% of all real fluid cells with a vanishing false positive fraction. For the reactive case,  $Y_{O_2} > 0.98$  captures 97% of the real fluid cells with a vanishing false positive fraction.

A real mixing model is required where a significant dilution of oxygen takes place under real fluid conditions. The drop-off of  $\phi_{\text{real}}^{\text{TP}}$  for higher  $Y_{O_2}^{\text{cutoff}}$  quantifies the presence of diluents in the oxygen stream. Figure 15 shows that a real fluid fraction of 0.03 is reached for  $Y_{O_2} > 0.8$  in the inert case, meaning that up to 20% diluent may be present in inert real fluid cells. In the reactive case, only 3%

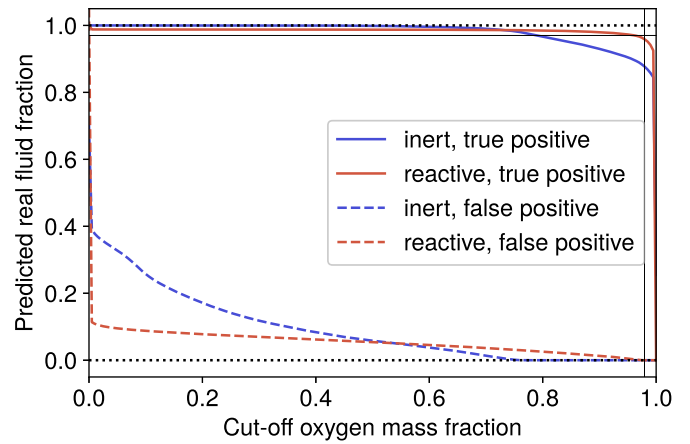


Fig. 15. Using  $Y_{O_2}^{\text{cutoff}}$  as real fluid prediction criterion for the inert and reactive shear layers. 'True positive' is the fraction of cells correctly identified as real, 'false positive' are cells that are ideal but misclassified as real. The vertical line marks  $Y_{O_2}^{\text{cutoff}} = 0.98$ , the horizontal line  $\phi_{\text{real}}^{\text{TP}} = 0.97$ .

diluent can be present in the real oxygen. Thus, in an answer to the second question, we see that under reactive conditions, mixing among real fluids only occurs marginally: oxygen transitions to an ideal state before significant mixing takes place. In the inert scenario, however, significant mixing with oxygen under real conditions can be observed.

## 4. Conclusions

The present paper investigates the thermodynamic structure of supercritical LOX/GH2 diffusion flames using 1D flame results and large eddy simulation. We deem the results relevant for technical systems in which LOX and GH2 are injected using coaxial injectors, e.g. the European Vulcain family of liquid propellant rocket engines, the Vinci upper stage engine, the U.S. Space Shuttle Main Engine (SSME), or the Japanese LE-5 series.

We found that mixing processes in high pressure injection are very different between inert and reactive cases. Specifically, we did not see the extent of real fluid mixing in reactive cases that we saw in inert cases. Instead, real fluid effects are confined to the LOX stream entering the chamber in a liquid state. Mixing takes place almost completely outside of this region under ideal gas conditions. Mixing among real fluids occurs but in a thin zone encapsulating the liquid oxygen; only water is found to mix with oxygen under real-fluid conditions, with a water mass fraction of about 3%.

In this sense, the structure of reactive supercritical injection is remarkably similar to a subcritical flame in which a strict separation between a pure oxygen stream and the surrounding ideal gas can be made.

We identify two thermodynamic transitions in transcritical non-premixed flames behind a coaxial injector: Cryogenic oxygen enters the chamber in a supercritical liquid state and undergoes (i) the pseudoboiling transition from a liquid to a gaseous state, and (ii) the subsequent transition to a supercritical ideal gas outside the flame. Both transitions occur approximately under pure fluid conditions.

A new representation of the local thermodynamic state in terms of reduced temperature and reduced pressure tracks each flame trajectory as the local composition changes, allowing for a clear interpretation and an intuitive assessment of the influence of changing operating conditions on the thermodynamic structure (injection temperatures, chamber pressure, dilution). In particular, water in the flame shifts the local critical point to higher pressures and temperatures, pushing the local state to subcritical pressures.

The results of this paper may lead to a new class of more efficient real fluid models in the future [20], which could be described as thermodynamic zonal models. Our results demonstrate that, dependent on the case, a real fluid equation of state is chiefly needed for pure oxygen and only in part of the flow field; real fluid mixing occurs but in a thin layer. Furthermore, real mixing in the reactive LOX/GH<sub>2</sub> case mainly occurs among O<sub>2</sub>/H<sub>2</sub>O and to a lesser extent for H<sub>2</sub>/H<sub>2</sub>O, with the potential to simplify the evaluation of the van der Waals mixing rules for detailed mechanisms. While all of this is captured with state-of-the-art models, accounting for real fluid behavior only where it is necessary may lead to significant reductions in computational cost.

## Acknowledgments

Financial support through NASA Marshall Space Flight Center is gratefully acknowledged. The authors would like to thank Dr. G. Lacaze for sharing his DNS data.

## References

- [1] J.C. Oefelein, R.N. Dahms, G. Lacaze, J.L. Manin, L.M. Pickett, Effects of pressure on fundamental physics of fuel injection in diesel engines, ICLASS, Heidelberg, Germany, 2012.
- [2] M. Oschwald, J.J. Smith, R. Branam, J. Hussong, A. Schik, B. Chehroudi, D. Talley, Injection of fluids into supercritical environments, *Combust. Sci. Technol.* 178 (2006) 49–100.
- [3] S. Candel, M. Juniper, G. Singla, P. Scoufflaire, C. Rolon, Structures and dynamics of cryogenic flames at supercritical pressure, *Combust. Sci. Technol.* 178 (2006) 161–192.
- [4] W. Mayer, H. Tamura, Propellant injection in a liquid oxygen/gaseous hydrogen rocket engine, *J. Propul. Power* 12 (6) (1996) 1137–1147.
- [5] J.A. Newman, T.A. Brzustowski, Behavior of a liquid jet near the thermodynamic critical region, *AIAA J.* 9 (8) (1971) 1595–1602.
- [6] R.C. Reid, J.M. Prausnitz, B.E. Poling, *The properties of gases and liquids*, 4th edition, McGraw Hill, 1987.
- [7] W. Mayer, A. Schik, V. Vielle, C. Chauveau, I. Gökalp, D.G. Talley, R.D. Woodward, Atomization and breakup of cryogenic propellants under high-pressure subcritical and supercritical conditions, *J. Propul. Power* 14 (1998) 835–842.
- [8] J. Manin, M. Bardi, L.M. Pickett, R.N. Dahms, J.C. Oefelein, Microscopic investigation of the atomization and mixing processes of diesel sprays injected into high pressure and temperature environments, *Fuel* 134 (2014) 531–543.
- [9] R.N. Dahms, J.C. Oefelein, Atomization and dense-fluid breakup regimes in liquid rocket engines, *J. Propul. Power* 31 (5) (2015) 1221–1231.
- [10] L. Qiu, R. Reitz, An investigation of thermodynamic states during high-pressure fuel injection using equilibrium thermodynamics, *Int. J. Multiph. Flow* 72 (2015) 24–38.
- [11] P. Gaillard, L. Matuszewski, V. Giovangigli, A diffuse interface LOX/hydrogen transcritical flame model, *Combust. Sci. Technol.* 20 (2016) 486–520.
- [12] J.M. P., R.N. Lichtenthaler, E.G. de Azevedo, *Molecular thermodynamics of fluid-phase equilibria*, 2nd edition, Prentice-Hall, 1985.
- [13] J.C. Oefelein, V. Yang, Modeling high-pressure mixing and combustion processes in liquid rocket engines, *J. Propul. Power* 14 (5) (1998) 843–857.
- [14] M. Juniper, N. Darabiha, S. Candel, The extinction limits of a hydrogen counterflow diffusion flame above liquid oxygen, *Combust. Flame* 135 (1–2) (2003) 87–96.
- [15] D. Lee, S. Thakur, J. Wright, M. Ihme, W. Shyy, Characterization of flow field structure and species composition in a shear coaxial rocket GH<sub>2</sub>/GO<sub>2</sub> injector: Modeling of wall heat losses, Proceedings of the 47th AIAA/ASME/SAE/ASEE Joint Propulsion Conference and Exhibit, AIAA, San Diego, USA (2011), pp. 2011–6125.
- [16] A. Urbano, L. Selle, G. Staffelbach, B. Cuenot, T. Schmitt, S. Ducruix, S. Candel, Exploration of combustion instability triggering using large eddy simulation of multiple injector liquid rocket engine, *Combust. Flame* 169 (2016) 129–140.
- [17] J.C. Oefelein, Thermophysical characteristics of shear-coaxial LOX–H<sub>2</sub> flames at supercritical pressure, *Proc. Combust. Inst.* 30 (2) (2005) 2929–2937.
- [18] V. Yang, Modeling of supercritical vaporization, mixing, and combustion processes in liquid-fueled propulsion systems, *Proc. Combust. Inst.* 28 (1) (2000) 925–942.
- [19] J.C. Oefelein, Mixing and combustion of cryogenic oxygen–hydrogen shear-coaxial jet flames at supercritical pressure, *Combust. Sci. Technol.* 178 (2006) 229–252.
- [20] D.T. Banuti, V. Hannemann, K. Hannemann, B. Weigand, An efficient multi-fluid-mixing model for real gas reacting flows in liquid propellant rocket engines, *Combust. Flame* 168 (2016) 98–112.
- [21] G. Ribert, N. Zong, V. Yang, L. Pons, N. Darabiha, S. Candel, Counterflow diffusion flames of general fluids: oxygen/hydrogen mixtures, *Combust. Flame* 154 (2008) 319–330.
- [22] L. Pons, N. Darabiha, S. Candel, G. Ribert, V. Yang, Mass transfer and combustion in transcritical non-premixed counterflows, *Combust. Theory Model.* 13 (1) (2008) 57–81.
- [23] G. Lacaze, J.C. Oefelein, A non-premixed combustion model based on flame structure analysis at supercritical pressures, *Combust. Flame* 159 (6) (2012) 2087–2103.
- [24] X. Wang, H. Huo, V. Yang, Supercritical combustion of general fluids in laminar counterflows, 51st AIAA Aerospace Sciences Meeting, Vol. 1165 (2013), 2013–1165.
- [25] H. Huo, X. Wang, V. Yang, A general study of counterflow diffusion flames at subcritical and supercritical conditions: oxygen/hydrogen mixtures, *Combust. Flame* 161 (12) (2014) 3040–3050.
- [26] X. Petit, G. Ribert, G. Lartigue, P. Domingo, Large-eddy simulation of supercritical fluid injection, *J. Supercrit. Fluids* 84 (2013) 61–73.
- [27] X. Petit, G. Ribert, P. Domingo, Framework for real-gas compressible reacting flows with tabulated thermochemistry, *J. Supercrit. Fluids* 101 (2015) 1–16.
- [28] U. Unnikrishnan, X. Wang, S. Yang, V. Yang, Subgrid scale modeling of the equation of state for turbulent flows under supercritical conditions, 53rd AIAA/SAE/ASEE Joint Propulsion Conference, AIAA, Atlanta, GA (2017), pp. 2017–4855.
- [29] S. Yang, Y. Li, U. Unnikrishnan, V. Yang, W. Sun, Comparison of tabulation and correlated dynamic evaluation of real fluid properties for supercritical mixing, 53rd AIAA/SAE/ASEE Joint Propulsion Conference, AIAA, Atlanta, GA (2017), pp. 2017–4858.
- [30] K. Nishikawa, I. Tanaka, Correlation lengths and density fluctuations in supercritical states of carbon dioxide, *Chem. Phys. Lett.* 244 (1995) 149–152.
- [31] F. Gorelli, M. Santoro, T. Scopigno, M. Krisch, G. Ruocco, Liquidlike behavior of supercritical fluids, *Phys. Rev. Lett.* 97 (2006) 245702.
- [32] M. Fisher, B. Widom, Decay of correlations in linear systems, *J. Chem. Phys.* 50 (9) (1969) 3756–3772.
- [33] V.V. Brazhkin, Y.D. Fomin, A.G. Lyapin, V.N. Ryzhov, K. Trachenko, Two liquid states of matter: a dynamic line on a phase diagram, *Phys. Rev. E* 85 (2012) 031203.
- [34] D.T. Banuti, M. Raju, M. Ihme, Similarity law for Widom lines and coexistence lines, *Phys. Rev. E* 95 (2017) 052120.
- [35] M. Raju, D.T. Banuti, P.C. Ma, M. Ihme, Widom lines and supercritical phase transitions of binary mixtures, *Sci. Rep.* 7 (2017) 3027.
- [36] D.T. Banuti, Crossing the Widom-line - Supercritical pseudo-boiling, *J. Supercrit. Fluids* 98 (2015) 12–16.
- [37] D.T. Banuti, K. Hannemann, The absence of a dense potential core in supercritical injection: a thermal break-up mechanism, *Phys. Fluids* 28 (3) (2016). 035103.
- [38] D.Y. Peng, D.B. Robinson, A new two-constant equation of state, *Ind. Eng. Chem. Res.* 15 (1) (1976) 59–64.
- [39] K.G. Harstad, R.S. Miller, J. Bellan, Efficient high-pressure state equations, *AIChE J.* 43 (6) (1997) 1605–1610.
- [40] P.J. Linstrom, W.G. Mallard, NIST chemistry webbook, in: NIST standard reference database number 69, National Institute of Standards and Technology, Gaithersburg, MD, (<http://webbook.nist.gov/chemistry>).
- [41] V. Giovangigli, L. Matuszewski, F. Dupoirieux, Detailed modeling of planar transcritical H<sub>2</sub>–O<sub>2</sub>–N<sub>2</sub> flames, *Combust. Sci. Technol.* 15 (2) (2011) 141–182.
- [42] J.P. Hickey, P.C. Ma, M. Ihme, S.S. Thakur, Large eddy simulation of shear coaxial rocket injector: real fluid effects, 49th AIAA/ASME/SAE/ASEE Joint Propulsion Conference, AIAA, San Jose, CA (2013), pp. 2013–4071.
- [43] P.C. Ma, Y. Lv, M. Ihme, An entropy-stable hybrid scheme for simulations of transcritical real-fluid flows, *J. Comput. Phys.* 340 (2017) 330–357.
- [44] P.C. Ma, D. Banuti, J.P. Hickey, M. Ihme, Numerical framework for transcritical real-fluid reacting flow simulations using the flamelet progress variable approach, 55th AIAA Aerospace Sciences Meeting, AIAA 2017–0143, Grapevine, TX (2017).
- [45] T.H. Chung, L.L. Lee, K.E. Starling, Applications of kinetic gas theories and multiparameter correlation for prediction of dilute gas viscosity and thermal conductivity, *Ind. Eng. Chem. Res.* 23 (1) (1984) 8–13.
- [46] T.H. Chung, M. Ajlan, L.L. Lee, K.E. Starling, Generalized multiparameter correlation for nonpolar and polar fluid transport properties, *Ind. Eng. Chem. Res.* 27 (4) (1988) 671–679.
- [47] S. Takahashi, Preparation of a generalized chart for the diffusion coefficients of gases at high pressures, *J. Chem. Eng. Jpn.* 7 (6) (1975) 417–420.
- [48] Y. Khalighi, J.W. Nichols, S. Lele, F. Ham, P. Moin, Unstructured large eddy simulation for prediction of noise issued from turbulent jets in various configurations, 17th AIAA/CEAS Aeroacoustics Conference, AIAA, Portland, OR (2011), pp. 2011–2886.
- [49] H. Terashima, M. Koshi, Approach for simulating gas–liquid-like flows under supercritical pressures using a high-order central differencing scheme, *J. Comput. Phys.* 231 (20) (2012) 6907–6923.
- [50] S. Gottlieb, C.W. Shu, E. Tadmor, Strong stability-preserving high-order time discretization methods, *SIAM Rev.* 43 (1) (2001) 89–112.
- [51] G. Strang, On the construction and comparison of difference schemes, *SIAM J. Num. Anal.* 5 (3) (1968) 506–517.
- [52] C.D. Pierce, P. Moin, Progress-variable approach for large-eddy simulation of non-premixed turbulent combustion, *J. Fluid Mech.* 504 (2008) 73–97.
- [53] M. Ihme, C. Cha, H. Pitsch, Prediction of local extinction and re-ignitions in non-premixed turbulent combustion using a flamelet/progress variable approach, *Proc. Combust. Inst.* 30 (2005) 793–800.
- [54] N. Peters, *Turbulent combustion*, Cambridge, 2000.
- [55] P.G. Robert, J.K. Michael, E. Coltrin, *Chemically reacting flow: theory and practice*, Wiley, 2003.

- [56] D.G. Goodwin, H.K. Moffat, R.L. Speth, Cantera: an object-oriented software toolkit for chemical kinetics, thermodynamics, and transport processes, 2016, <http://www.cantera.org>, version 2.2.1.
- [57] R.N. Dahms, L.M. Pickett, J.C. Oefelein, A dense fluid approximation for the simulation of diesel engine fuel injection processes, ILASS Americas, Ventura, CA, 2011.
- [58] K. Harstad, J. Bellan, The Lewis number under supercritical conditions, *Int. J. Heat Mass Transf.* 42 (6) (1999) 961–970.
- [59] A.M. Ruiz, G. Lacaze, J.C. Oefelein, R. Mari, B. Cuenot, L. Selle, T. Poinso, Numerical benchmark for high-reynolds-number supercritical flows with large density gradients, *AIAA J.* 54 (5) (2015) 1445–1460.